An approach to wide-field imaging of linear rail ground-based SAR in high squint multi-angle mode

ZHANG Yuan[1], ZHANG Qiming[1], WANG Yanping[1,*], LIN Yun[1], LI Yang[1],
BAI Zechao[1], and LI Fang[2]

1. School of Information Science and Technology, North China University of Technology, Beijing 100144, China;
2. Quanzhou Institute of Equipment Manufacturing, Haixi Institutes, Chinese Academy of Sciences, Jinjiang 362200, China

Abstract: Ground-based synthetic aperture radar (GB-SAR) has been successfully applied to the ground deformation monitoring. However, due to the short length of the GB-SAR platform, the scope of observation is largely limited. The practical applications drive us to make improvements on the conventional linear rail GB-SAR system in order to achieve larger field imaging. First, a turntable is utilized to support the rotational movement of the radar. Next, a series of high-squint scanning is performed with multiple squint angles. Further, the high squint modulation phase of the echo data is eliminated. Then, a new multi-angle imaging method is performed in the wave number domain to expand the field of view. Simulation and real experiments verify the effectiveness of this method.

Keywords: ground-based synthetic aperture radar (GB-SAR), high squint, multi-angle.

1. Introduction

Synthetic aperture radar (SAR) has been widely applied in many aspects of earth observation by spaceborne or airborne platforms. Usually spaceborne platforms are used to perform monitoring periodically, while in an emergency the airborne platform is dispatched to do local surveillance. Although this traditional operation mode has greatly improved our observation ability, in practical experience, considering factors such as scheduling and revisit times, it is still insufficient for repeat observations that are often needed for local small-scale areas, e.g., for landslide or infrastructure monitoring, where both spaceborne and airborne SAR come to their limitations due to the lack of flexibility. Under these circumstances, a SAR platform with rapid response and repeated local observation be-

comes a desired tool.

As an important complement, ground based-SAR (GB-SAR) can achieve more accurate and efficient results than satellites or airborne SAR systems in local environments, and is increasingly concerned by civilian applications. The currently disclosed linear rail GB-SAR system includes Tohoku University's ground-based interferometric system at Ku band, which successfully monitored the landslide of Aratozawa [1]. University of Florence's continuous-wave step frequency radar at C-band monitored the slow movement of Glacier with the scan time of 36 min [2]. The Polytechnic University of Catalonia used the X-band system to make long-term observations of the slow movement of the mountain and obtained the corresponding moving speed [3]. Researchers from the European Commission used the multiple input multiple output (MIMO) mode to replace the way the radar moves along the rail, and compared it with previous systems at 13.85 GHz [4]. Temesgen et al. developed the X-band Tomographic mode GB-SAR for near-range measurement of ice thickness [5]. The systems listed here are some of the outstanding representative results, but GB-SAR systems are not limited to these.

Compared with the conventional SAR, the significant difference in imaging of the GB-SAR system is that the synthetic aperture is limited by the platform length, so it cannot form a complete aperture, also called suboptimal aperture [6]. However, since the radar platform is completely stationary, the main advantage of GB-SAR imaging is that the platform motion speed is more stable during data acquisition. Therefore, the accuracy of deformation monitoring is much higher, which is generally considered to be millimeter-level. Moreover, it can be used for long-term monitoring of local areas, such as bridge monitoring [7], discontinuous monitoring of slow deformation [8], iron open pit monitoring [9], post-earthquake damage inspection [10], evaluation of snow-mass characteris-

tic [11], post-landslide monitoring [12], subsidence phenomenon in urban environment [13], atmospheric correction [14], height-dependent atmospheric artifacts compensation [15], soil surface roughness characterization [16], and castle cliff monitoring [17].

Since GB-SAR has the above characteristics, the research community has carried out research on related imaging algorithms from the beginning. Joaquim et al. proposed a fast pseudo-polar format imaging algorithm for far-field scenarios [18], which is improved further for near-field imaging [19]. ZENG et al. proposed keystone formatting technique to solve the problem of space-variant range cell migration correction (RCMC) [20]. Reale et al. addressed the use of multi-baseline ground-based data for the reconstruction of the three-dimensional backscattering properties [21]. The above-mentioned methods make approximations of the slant-range. Thus, Monti Guarnieri et al. introduced the wave number domain focusing algorithm into the GB-SAR system [22]. Guo et al. proposed a similar method for GB-SAR imaging in the frequency modulated continuous wave (FMCW) mode [23]. Most GB-SAR systems have been used in the step-frequency mode in the past [24]. In this mode, the radar is almost perfectly stationary when receiving the echo signal, which helps to improve the coherence, but in actual use, this mode costs too much acquisition time, usually in about tens of minutes. In the FMCW mode, the radar collects data while moving, thereby improving the efficiency of data acquisition. Therefore, this paper uses the FMCW mode that can complete scanning within one minute.

Actual systems are typically deployed within 5 km from the observation scene. For the system in this paper, it has an azimuth beam angle of β and a moving speed v as shown in Fig. 1. Here, the azimuth beam angle is defined as the angle of the antenna azimuth pattern at -3 dB. Since the platform limits the synthetic aperture length, the system also has a limited imaging field of view. One solution to the expansion of the field of view is to use the Arc-SAR system [25,26]. However, this kind of system requires additional long rotating arm (usually 1 m to 2 m) for the antenna to form the synthetic aperture in the circular scanning mode. Moreover, the Arc-SAR system uses the circular imaging methods, which makes the system processing more complex. Without considering the development of a new Arc-SAR system, for users who have already deployed the linear rail GB-SAR, can they continue to use the original system and expand the scope of monitoring? This is not only meaningful from a research perspective, but also very useful for actual users to control their costs.

This paper proposes a high squint multi-angle imaging approach of linear rail GB-SAR for larger fields of view. First, a turntable is installed on the bracket to support the radar. After that, the scanning with various squint angles of the observed area is performed. Then, we make joint imaging of the multi-angle echo data in the wave number domain. Finally, after expanding the field of view, the corresponding imaging results can be further used for the differential interferometry.
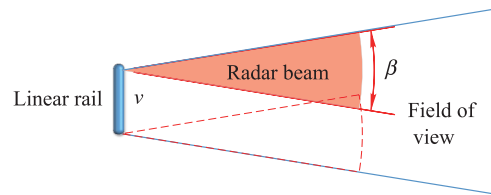

Fig. 1   Imaging scope of conventional GB-SAR

2. High squint multi-angle scanning in improved GB-SAR system

In this section, the radar is mounted on a rotatable bracket that can point at any angle controlled by the computer. The scanning process is shown in Fig. 2. It scans M times in squint angles of $\theta_1, \theta_2, \ldots, \theta_M$, respectively. We define the angle between the direction of motion and the direction of the LOS of the radar as squint angle θ_i. The subscript number, i.e., $i = 1, 2, \ldots, M$ in respective $\theta_1, \theta_2, \ldots, \theta_M$, represents the different squint angles in a scanning group. Within a single scanning pass, the squint angle keeps unchanged. When the radar is in the return trip after scanning, the system will quickly change the squint angle, so that in the next scanning it can adopt the new squint angle. Then, these M times echo data are formed as Group 1 to generate Image 1 by the multi-angle joint imaging method. Then, the above process will be repeated to generate Image 2, Image 3, ..., Image M.
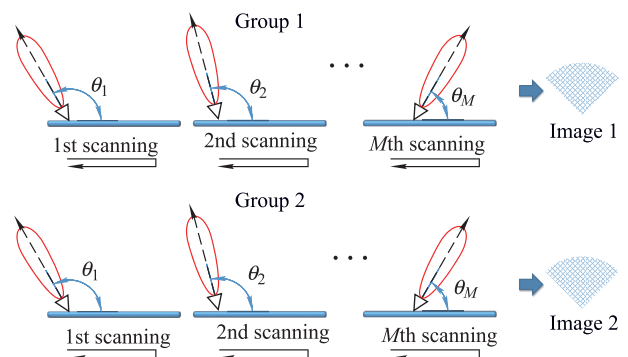

Fig. 2   Scanning process of the improved GB-SAR system

In the interferometry processing, we use the image pairs with the same squint angle, as shown in Fig. 3. For example, the data of the squint angle θ_1 in each group are used for the interferometric process to generate a deformation map at the direction θ_1. The data of the squint angle θ_2 in

each group are used for the interferometric process to generate a deformation map at the direction θ_2, and so on. The interferogram is formed by fan-shaped regions according to the number of squint angles.
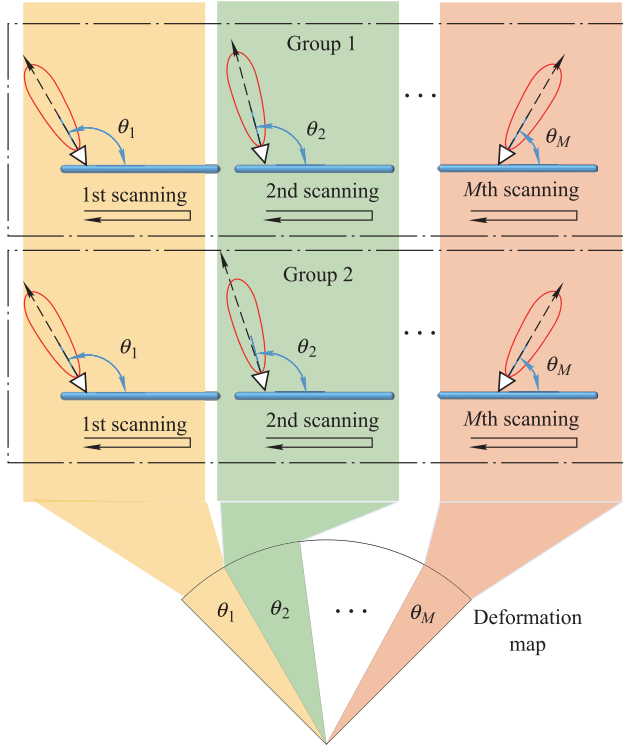

Fig. 3   Interferometry processing flow

The deformation map is composed of multiple data with different squint angles by stitching, so the field of view will be much larger than that in the conventional linear mode system. And the difference between each adjacent squint angles is usually less than the system azimuth beam angle β, so there is no blind zone between the boundaries of each sector data. Finally, we can get a larger deformation map than the original system.

Through the above processing, the system will have the ability of a significant expansion of the observation area by making minor changes to the original linear rail GB-SAR system. Compared with the original system, since the improved one makes scanning with several squint angles, we need further study the imaging method for multi-angle echo data. It should be noted that the enlargement of the field of view is due to the fact that the radar can be pointed in different squint directions with the help of the rotating bracket. On this basis, the problem of joint imaging of multiple echo data with different squint angles is the focus of this paper.

3. High squint multi-angle imaging algorithm

Fig. 4 shows a data acquisition geometry diagram with the squint angle. Here we define the angle between the direction of motion and the direction of the line of sight (LOS) of the radar as squint angle θ. The radar speed is v, and the scanning time along the platform is T_a. The current azimuth sampling time is t. r_c is the distance between the scene center and the radar position at $t = 0$. The coordinate of the scene center is $(r_c \cos\theta, r_c \sin\theta)$, the point target locates at $(x, y) = (r_c \cos\theta + x_0, r_c \sin\theta + y_0)$, and the radar is at $(vt, 0)$. Therefore, the slant-range can be expressed as
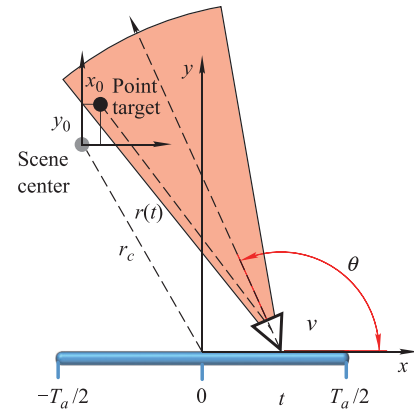
$$r(t) = \sqrt{(x - vt)^2 + y^2}. \tag{1}$$

Fig. 4   High squint data acquisition geometry

The transmitted signal is

$$s(\tau) = \text{rect}\left(\frac{\tau}{T_p}\right) \cdot \exp\{j(2\pi f_0\tau + \pi K_r\tau^2)\} \tag{2}$$

where τ is the range time, T_p is the time width of the transmitted signal, f_0 is the carrier frequency, and K_r is the chirp rate. The slant-range represented by (1) induces a time delay in the range shown below:

$$\tau_p = \frac{2r(t)}{c} \tag{3}$$

where c is the velocity of light. τ_p contains the squint angle θ.

Thus, the echo signal can be written as

$$ss(t, \tau; \theta) = \text{rect}\left(\frac{\tau - \tau_p}{T_p}\right) \cdot \text{rect}\left(\frac{t}{T_a}\right) \cdot$$

$$\exp\{j[2\pi f_0(\tau - \tau_p) + \pi K_r(\tau - \tau_p)^2]\} \tag{4}$$

where t is the time in the azimuth, T_a is the scanning time along the azimuth. Assume that the scattering coefficient is a unit value. The relationship between the transmitted signal and the received signal is displayed in a time-frequency manner as shown in Fig. 5.
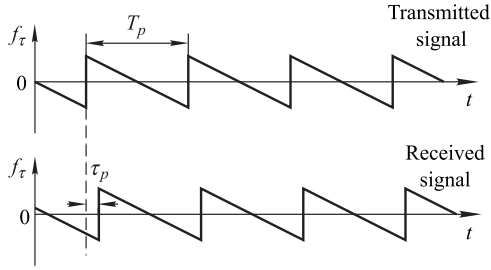
Fig. 5   Relationship between the transmitted signal and the received signal

We use the 'Dechirp-on-receive' technique to reduce the sampling requirements by mixing the received and transmitted signals [27]. And the output of the mixer is then low-pass filtered before being sampled. Echoed signals from the scene of interest usually have high frequencies resulting from the characteristics of the FMCW system. In order to demodulate the frequency spectrum of echo signals to the baseband, the reference signal with delay time of τ_c is given by

$$s_{ref} = \exp\{j[2\pi f_0(\tau - \tau_c) + \pi K_r(\tau - \tau_c)^2]\} \quad (5)$$

where $\tau_c = 2r_c/c$ is the time delay of the reference signal. The dechirped signal can be expressed as

$$ss_{IF}(t, \tau; \theta) = ss(t, \tau; \theta) \cdot s_{ref}^* =$$

$$\text{rect}\left(\frac{\tau_d - \tau_\Delta}{T_p}\right) \cdot \text{rect}\left(\frac{t}{T_a}\right) \cdot \exp\{-j(\pi K_r \tau_\Delta^2)\}\cdot$$

$$\exp\{j(-2\pi f_0 \tau_\Delta - 2\pi K_r \tau_d \tau_\Delta)\} \quad (6)$$

where $\tau_d = \tau - \tau_c$ and $\tau_\Delta = \tau_p - \tau_c$. $*$ represents the complex conjugate.

In the actual system, the dechirped signal is acquired as a digital signal by the A/D converter. For ease of derivation, the continuous signal form is still used later. In (6), the last exponential term is well-known as the residual video phase (RVP). It could be eliminated by a method named 'Deskew', which comprises Fourier transform (FT), phase multiplication, and inverse FT [27,28]. After the RVP removal, we obtain

$$ss_{IF}(t, \tau_d; \theta) = \text{rect}\left(\frac{\tau_d}{T_p}\right) \cdot \text{rect}\left(\frac{t}{T_a}\right) \cdot$$

$$\exp\{j(-2\pi f_0 \tau_\Delta - 2\pi K_r \tau_d \tau_\Delta)\}. \quad (7)$$

Performing the time-frequency substitution of $f_r = K_r \tau_d$ yields

$$ss(t, f_r; \theta) = \text{rect}\left(\frac{f_r}{B_r}\right) \cdot \text{rect}\left(\frac{t}{T_a}\right) \cdot$$

$$\exp\{j[-2\pi(f_0 + f_r)\tau_\Delta]\} \quad (8)$$

where B_r is the bandwidth of the transmitted signal. The above process is a common pre-processing step of FMCW-SAR. In order to ensure the integrity, we still write it out. Note that τ_Δ contains the squint angle θ. The phase in (8) can be written as

$$\Phi_t = \frac{4\pi}{c}(f_0 + f_r)r_c - \frac{4\pi}{c}(f_0 + f_r)\cdot$$

$$\sqrt{(r_c \cos\theta + x_0 - vt)^2 + (r_c \sin\theta + y_0)^2}. \quad (9)$$

Next, we perform the FT of (9) along the azimuth direction. Note that for the suboptimal aperture data, it requires a zero padding for echoes to satisfy the azimuth size of the scene [22]. After that, according to the principle of the stationary phase, the phase in the wave number domain can be expressed by

$$\Phi = -2\pi k_\theta r_c + 2\pi k_r r_c + 2\pi k_a x_0 - 2\pi k_r y_0 \cos\phi \quad (10)$$

where

$$\begin{cases} k_a = -\dfrac{f_a}{v} \\ k_r = \dfrac{f_0 + f_r}{c/2} \end{cases}. \quad (11)$$

To understand (10), we refer to Fig. 6. It is a local approximation of the spherical wave. This approximation is reasonable in the local region around the radar line of sight. θ is the squint angle. λ is the wavelength in the plane wave propagation direction. λ_x and λ_y is the wavelength in the x and y direction. ϕ is the angle between λ and λ_y. And the projection of λ in the squint direction is λ_θ.

$$\begin{cases} 1/\lambda^2 = 1/\lambda_y^2 + 1/\lambda_x^2 \\ \lambda_x = 1/k_a \end{cases} \quad (12)$$

$$\lambda_\theta = \frac{\lambda}{\sin(\theta - \phi)} \quad (13)$$
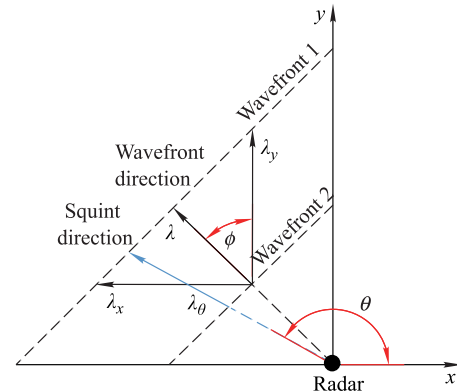
$$k_\theta = 1/\lambda_\theta \quad (14)$$

Fig. 6   Plane wave geometric diagram in squint case

Equation (14) is the wave number in the squint direction that contains the coupling term of the range frequency and the azimuth frequency as well as the squint modulation term. It determines the first term in (10).

The complete expression of the signal in the two-dimensional (2D) wave number domain is

$$SS(k_a, k_r; \theta) = W(k_a, k_r) \cdot e^{j \cdot \Phi} \qquad (15)$$

where $W(k_a, k_r)$ is the amplitude in the 2D wave number domain. The imaging process is further discussed below.

From (10), (13) and (14), we can get

$$\Phi = -2\pi k_r r_c \sin(\theta - \phi) + 2\pi k_r r_c +$$

$$2\pi k_a x_0 - 2\pi k_r y_0 \cos\phi. \qquad (16)$$

Since r_c is a known term, we compensate the first order of wave number k_r at first.

$$SS_1(k_a, k_r; \theta) = SS(k_a, k_r; \theta) \cdot \exp\{-j(2\pi k_r r_c)\} =$$

$$W(k_a, k_r) \cdot \exp\{-j[2\pi k_r r_c \sin(\theta - \phi)]\} \cdot$$

$$\exp\{j(2\pi k_a x_0 - 2\pi k_r y_0 \cos\phi)\} \qquad (17)$$

The second phase term in (17) is the first order of wave number k_a that determines the target position. The first phase term is mainly derived from the squint effect, which can be compensated by

$$SS_2(k_a, k_r; \theta) = SS_1(k_a, k_r; \theta) \cdot$$

$$\exp\{j[2\pi k_r r_c \sin(\theta - \phi)]\} =$$

$$W(k_a, k_r) \cdot \exp\{j(2\pi k_a x_0 - 2\pi k_r y_0 \cos\phi)\}. \qquad (18)$$

After the compensation, the squint modulation in the phase is eliminated. Note that (i) ϕ changes with k_a and k_r, so this item should be compensated in the pointwise way. (ii) $SS_2(k_a, k_r; \theta)$ implies the squint angle θ. For example, the actual data in our system contains multiple angles, such as the M angles shown in Fig. 3. Therefore, each angle data should be compensated according to its squint angle. Moreover, the squint causes the Doppler center frequency offset. The azimuth wave number center is

$$k_{ac} = -2/\lambda \cdot \cos\theta. \qquad (19)$$

The first phase term in (18) is the first order of the azimuth wave number k_a, which determines the azimuth position of the target in the image, and does not affect the focusing. The second phase term is the coupling term of the wave number k_a and the wave number k_r in the propagation direction. Equation (18) can be further transformed into

$$SS_2(k_a, k_r; \theta) = W(k_a, k_r) \cdot$$

$$\exp\{-j(2\pi y_0 \sqrt{k_r^2 - k_a^2})\} \cdot \exp\{j(2\pi k_a x_0)\}. \qquad (20)$$

Since the system has multiple angle data, we keep the squint angle θ in the left-hand variable as a marker of different angles. We perform the Stolt interpolation of $\widehat{k}_r = \sqrt{k_r^2 - k_a^2}$ to (20), and it becomes

$$SS_3(k_a, \widehat{k}_r; \theta) = W(k_a, \widehat{k}_r) \cdot$$

$$\exp\{-j(2\pi \widehat{k}_r y_0)\} \cdot \exp\{j(2\pi k_a x_0)\}. \qquad (21)$$

Note that we perform Stolt interpolation to all multi-angle data simultaneously, and finally the data are coherently accumulated into a data matrix, which is denoted as

$$SS_{\text{Total}}(k_a, \widehat{k}_r) = \sum_\theta SS_3(k_a, \widehat{k}_r; \theta). \qquad (22)$$

And in actual engineering, it can be implemented by the parallel algorithm. After the above processing, the wave numbers corresponding to the squint angles θ_1, $\theta_2, \ldots, \theta_M$ are substantially projected to two mutually orthogonal wave numbers of $\widehat{k}_r$ and k_a, which have the wavelength of λ_x and λ_y, respectively, as shown in Fig. 7.

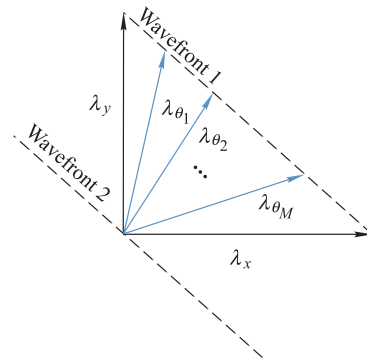**Fig. 7   Multi-angle wave numbers geometry**

In the end, the inverse FT is performed on the signal of (22) to obtain a focused image,

$$ss(x, y) = F^{-1}\{SS_{\text{Total}}(k_a, \widehat{k}_r)\} =$$

$$W_x(x - x_0) \cdot W_y(y - y_0) \qquad (23)$$

where F^{-1} represents the inverse FT. $W_x(\cdot)$ and $W_y(\cdot)$ are the envelope functions in the azimuth and the range, respectively. They are determined by the system ambiguity function. The entire algorithm flow is shown in Fig. 8.
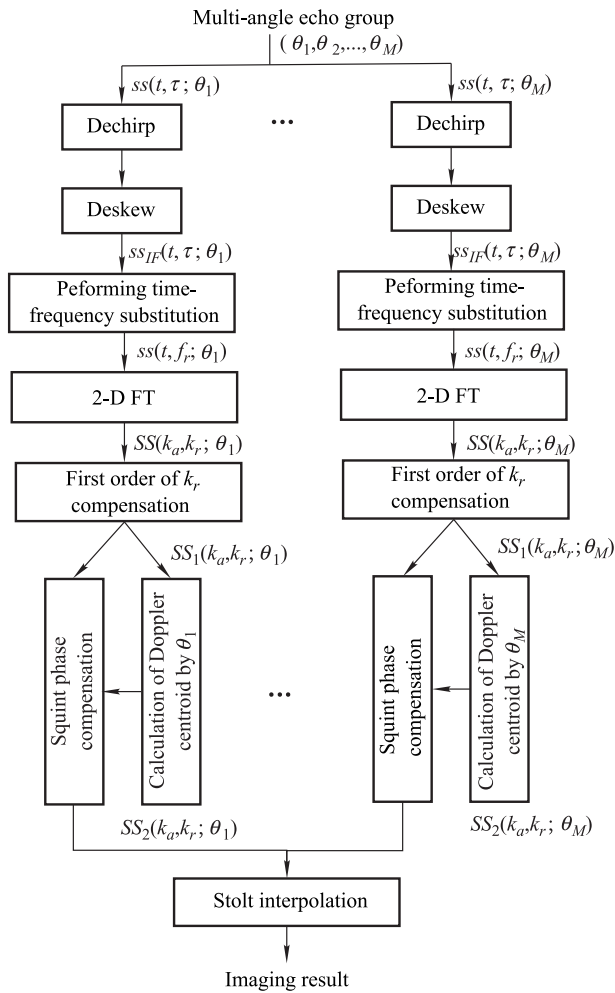
Multi-angle echo group
$(\theta_1, \theta_2, ..., \theta_M)$

$ss(t, \tau; \theta_1)$

| Dechirp | ... | Dechirp |

$ss(t, \tau; \theta_M)$

| Deskew | | Deskew |

$ss_{IF}(t, \tau; \theta_1)$ ... $ss_{IF}(t, \tau; \theta_M)$

| Peforming time-frequency substitution | | Peforming time-frequency substitution |

$ss(t, f_r; \theta_1)$ ... $ss(t, f_r; \theta_M)$

| 2-D FT | | 2-D FT |

$SS(k_a, k_r; \theta_1)$ ... $SS(k_a, k_r; \theta_M)$

| First order of k_r compensation | | First order of k_r compensation |

$SS_1(k_a, k_r; \theta_1)$ ... $SS_1(k_a, k_r; \theta_M)$

Squint phase compensation / Calculation of Doppler centroid by θ_1 ... Squint phase compensation / Calculation of Doppler centroid by θ_M

$SS_2(k_a, k_r; \theta_1)$ ... $SS_2(k_a, k_r; \theta_M)$

| Stolt interpolation |

Imaging result

Fig. 8   Flow chart of high squint multi-angle imaging algorithm

4. Simulation and real data experiments

The system parameters are shown in Table 1. The antenna pattern used in this paper is shown in Fig. 9, and the corresponding angle of the E plane response at −3 dB is 18° which is the azimuth beam angle. Section 4.1 analyzes the performance of the algorithm through simulation. Section 4.2 shows the deformation measurement experiment in the laboratory. Section 4.3 shows the actual test scenario and the results of the actual data processing.

Table 1   System parameters

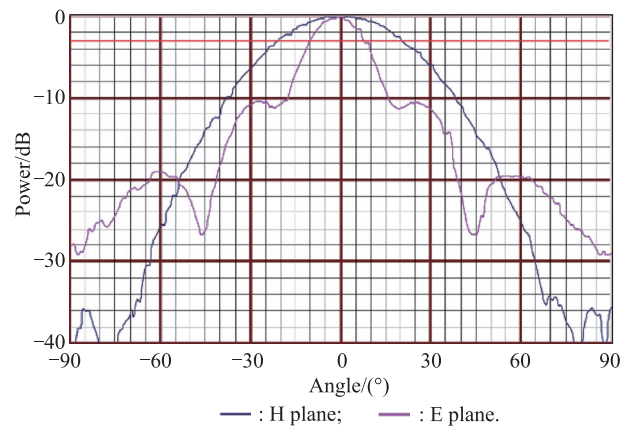| Parameter	Value
Carrier frequency/GHz	17.5
Platform length/m	2
Radar velocity/(m/s)	0.03
Angle of azimuth beam/(°)	18
Transmitted bandwidth/MHz	500
Sampling frequency/MHz	50
Azimuth resolution/m	0.70
Slant-range/m	200
Range resolution/m	0.30

Fig. 9   Antenna gain diagram

4.1   Performance analysis by simulation

Firstly, the RCMC analysis is performed on the scene center point according to different squint angles. Fig. 10(a) shows the linear component of RCMC. It can be seen that as the squint increases, the contribution of this item to RCMC increases significantly. Within the suboptimal aperture time, the linear component can exceed the range resolution.
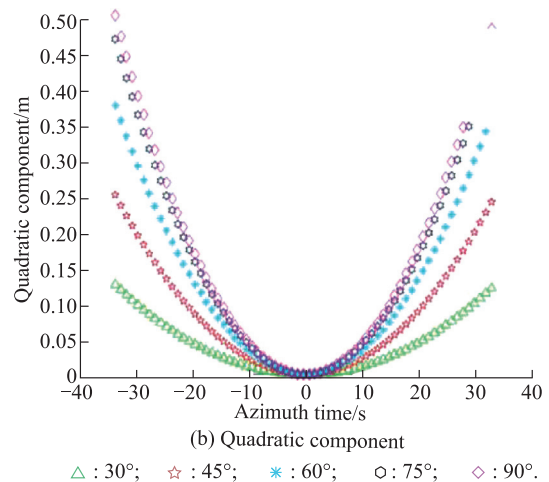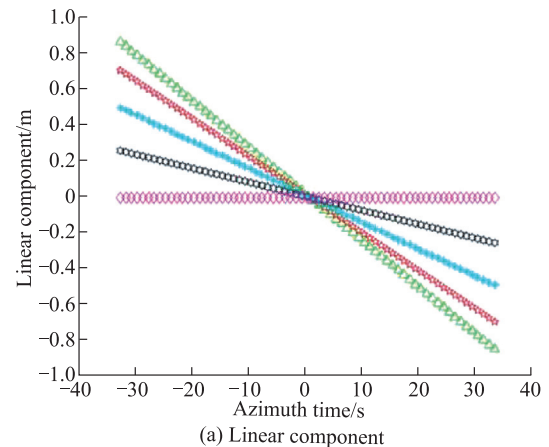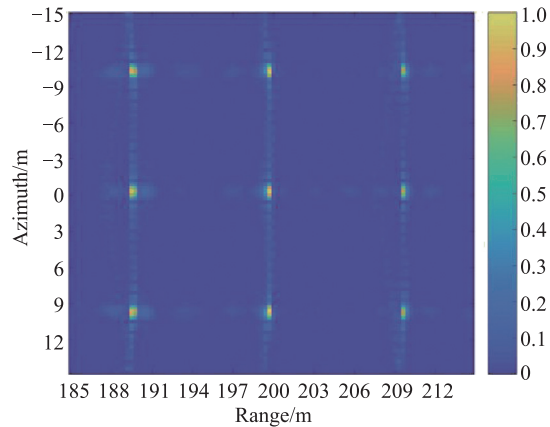

(a) Linear component

(b) Quadratic component

△ : 30°;   ☆ : 45°;   ✳ : 60°;   ○ : 75°;   ◇ : 90°.

Fig. 10   RCMC analysis on the scene center

Fig. 10(b) shows the quadratic component of RCMC. It can be seen that as the squint state increases, this term decreases. In most squint cases, the quadratic components are basically smaller than the range resolution. However, when approaching the side-looking, the quadratic component must be considered for compensation. The algorithm in this paper does not perform any approximation on the slant-range, and can fully compensate for the linear and quadratic components at any squint angle.

Next, we verify the performance of this method through single squint angle experiments. We set the 3×3 lattices arranged equidistantly in the scene. The distance of the scene center is 200 m. The imaging results with squint angles of 90°, 105° and 120° are simulated respectively, and the corresponding imaging results are shown in Fig. 11(a), Fig. 12(a) and Fig. 13(a), respectively. The back projection (BP) algorithm is a time-domain high-precision imaging method [29]. Although the algorithm is very time-consuming, it is often used as a comparison method. Therefore, we use BP for comparison imaging. BP imaging results are shown in Fig. 11(b), Fig. 12(b) and Fig. 13(b), respectively. Due to symmetry, results at $\theta = 60°$, $\theta = 75°$ are omitted.

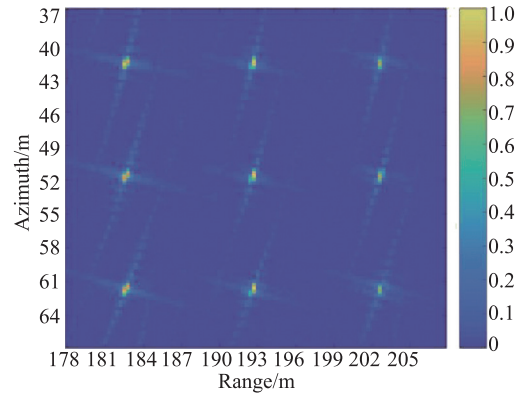(a) Result by the proposed method

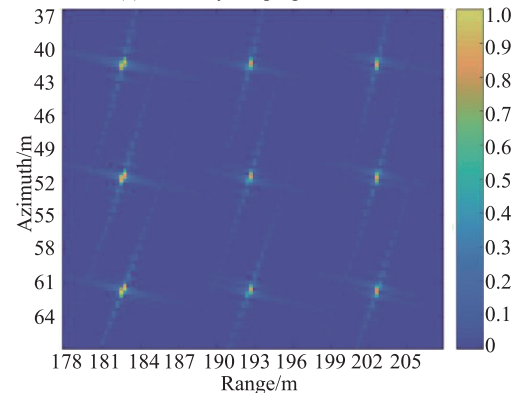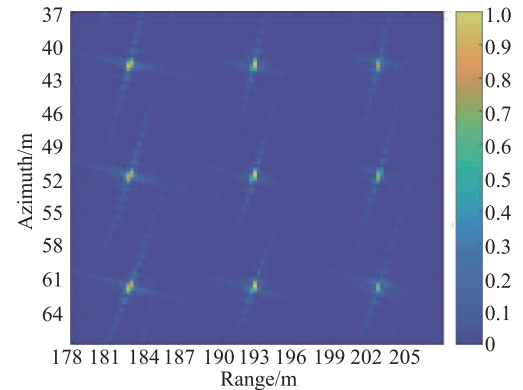(b) Result by BP

Fig. 12 Imaging results at $\theta=105°$
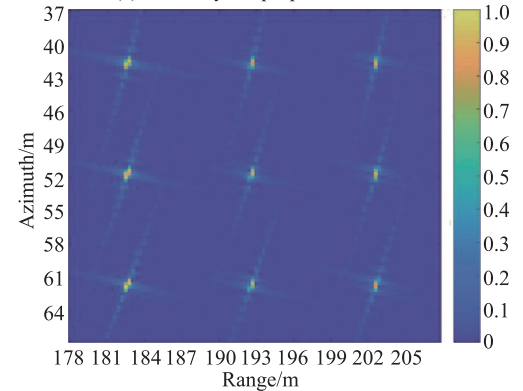

(a) Result by the proposed method

(a) Result by the proposed method
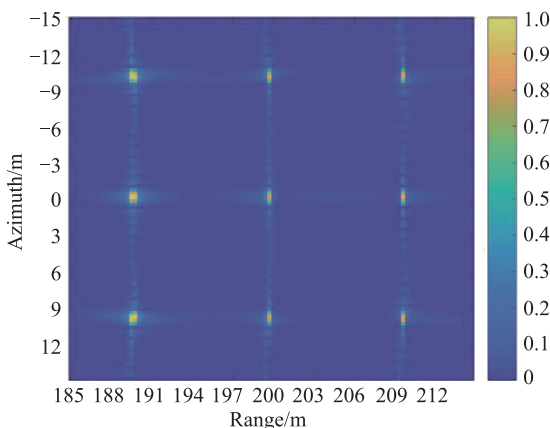
(b) Result by BP

Fig. 11 Imaging results at $\theta=90°$

(b) Result by BP

Fig. 13 Imaging results at $\theta=120°$

From the comparison between Fig. 11(a) and Fig. 11(b), Fig. 12(a) and Fig. 12(b), Fig. 13(a) and Fig. 13(b), it can be seen that the imaging position of this method is consistent with the BP method under different squint angles, and no obvious geometric deformation occurs. Table 2 gives an analysis comparison of these imaging results. We select the azimuth resolution ρ_a and the azimuth peak sidelobe ratio (PSLR) of the center point in each image as comparison parameters. Because the range processing of the two methods is consistent, only the azimuth parameters are compared. In general, it can be seen that the method in this paper is close to the BP imaging results.

Table 2   Analysis comparison of imaging results

θ	The proposed method		BP	
	ρ_a/m	PSLR	ρ_a/m	PSLR
60°	0.78	−13.0	0.70	−13.2
75°	0.76	−13.2	0.71	−13.2
90°	0.73	−13.2	0.70	−13.2
105°	0.72	−13.2	0.70	−13.2
120°	0.80	−13.0	0.70	−13.2

Usually in the airborne SAR system, since the system has a limited pulse repetition frequency (PRF) and the platform moves at a high speed, high squint can cause Doppler ambiguity. However, in our GB-SAR system, due to the slow motion of the radar, e.g., 0.03 m/s in this paper, the Doppler frequency center does not exceed the PRF, so this paper does not consider the Doppler ambiguity problem.

The simulation experiment of a large-scale scene is done below, and the point targets are arranged at intervals of 20 m in a range of 200 m × 200 m with a center distance of 200 m, as shown in Fig. 14.
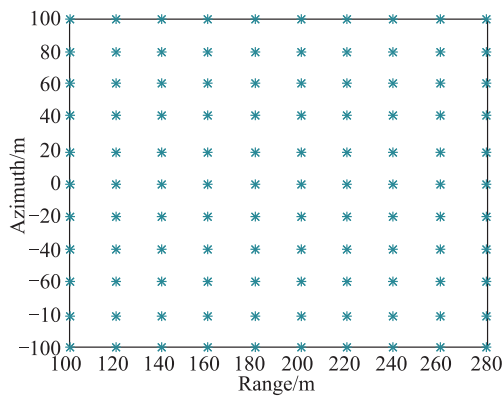

Fig. 14   Scene layout for large scene simulation

First, we simulate the data acquisition process of a conventional system and use the BP imaging algorithm. The imaging results are shown in Fig. 15(a). Since the conventional system has bounded the beam angle, there are blind areas in the field of view. Only a part of point targets in the scene is displayed. Then, we simulate the data acquisition process of the improved system and perform imaging by this algorithm. The result is shown in Fig. 15(b).

Compared with the conventional system, for the same observation scene, the field of view imaged by the improved system is larger.
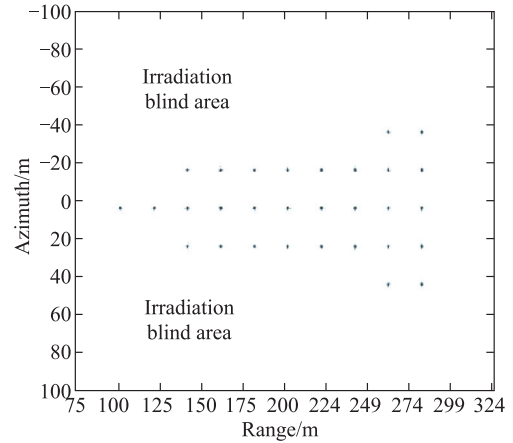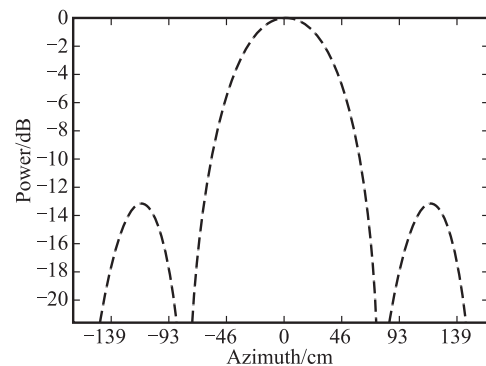

(a) Conventional system
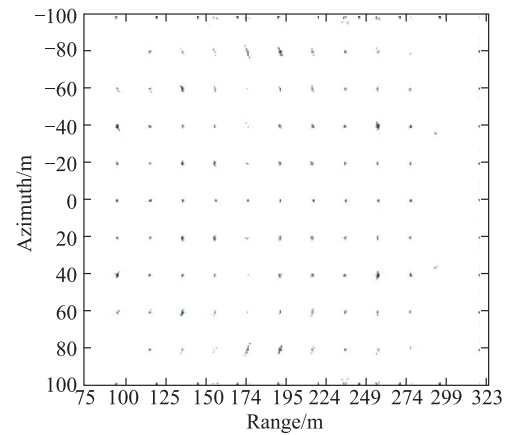
(b) The improved system

Fig. 15   Large scene simulation imaging results

The simulated point targets in the whole scene are all displayed. We select one of the point targets for focus quality analysis as shown in Fig. 16. The measured azimuth and range resolutions are 0.70 m and 0.30 m, respectively.
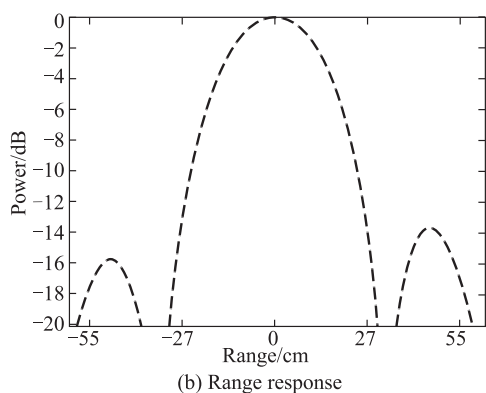

(a) Azimuth response

(b) Range response

Fig. 16   Point target response analysis after imaging by the proposed method

### 4.2   Deformation measurement of indoor experiment

The indoor experimental scene is shown in Fig. 17. A corner reflector is placed in the scene with 2.5 m from the radar.
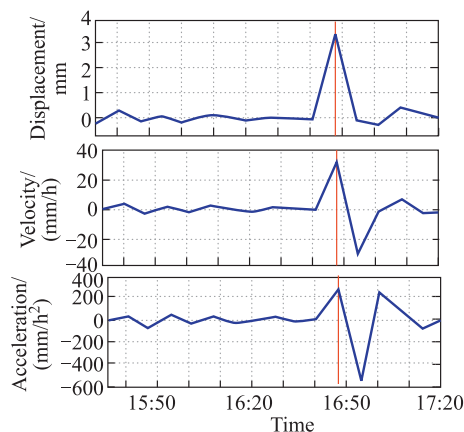

Fig. 17   Indoor deformation test scene

The multi-angle scanning is performed at 75°, 90° and 105° for an observation time of 2 h. During the interval of scanning, we artificially moved the corner reflector about 3 mm. Fig. 18(a) is the SAR image of the corner reflector. The deformation is represented by Fig. 18(b). And 16:50 indicates the point in time when the deformation occurs. Before and after this time, the deformation is close to 0 mm. Moreover, the two pictures below the deformation figure are the speed and acceleration of deformation change with time, respectively. It can be seen from the experimental results in Fig. 18 that the displacement around

16:50 suddenly reaches 3 mm, and then quickly drops to around 0 mm, which coincides with the fact.
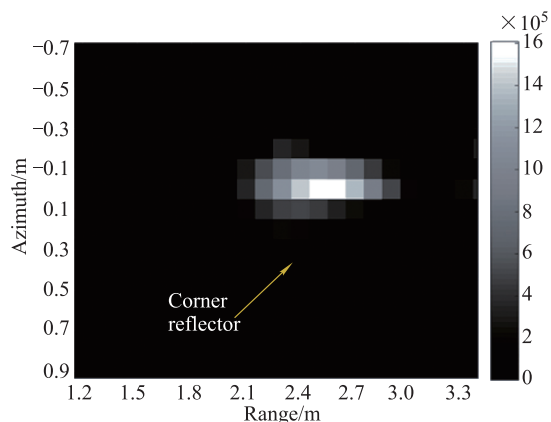
(a) SAR image of the corner reflector

(b) Deformation

Fig. 18   Indoor deformation test results

4.3   High squint multi-angle imaging experiment for large-scale infrastructure construction

The Yongding River Bridge is currently under construction in Beijing. The design sketch is shown in Fig. 19, which shows the full view of the bridge after it is completed. The bridge length is about 600 m, which belongs to the double tower diagonal-pull type. The heights of the two towers are 120 m and 73 m, respectively.

Fig. 19   Design sketch of Yongding River Bridge

In Fig. 19, the bridge pier corresponds to the observation object in Fig. 20 that is the current status of the bridge during on-site observation. The radar placement position can also be seen in Fig. 20.

Fig. 20   Field experiment scene

The system after installing the turntable is shown in Fig. 21. The angle of the turntable can be controlled by the computer and set to a new angle during the return of radar on the platform after scanning. We use the conventional side-looking mode and propose the multi-angle mode to monitor the Yongding River Bridge, seperatley. In the multi-angle imaging mode, each group of squint angles includes $\theta = 60°$, $75°$, $90°$, $105°$ and $120°$. After imaging by this method, the overall outline of the bridge is clearly visible.

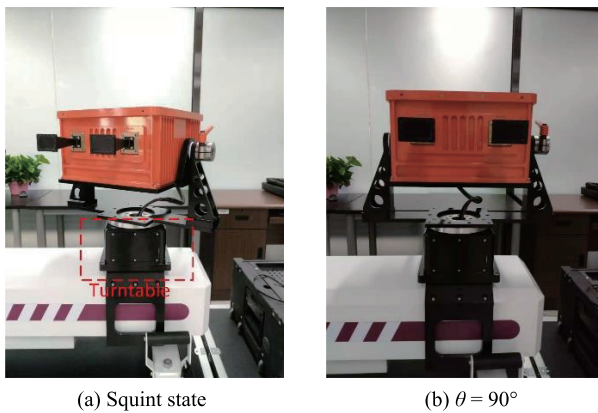(a) Squint state   (b) $\theta = 90°$

Fig. 21   Improved GB-SAR with radar turntable

Fig. 22 is the amplitude image of the large field of view of the bridge obtained by the method in this paper. This does not represent the deformation of the bridge. Deformation inversion needs to be obtained by differential interferometry on the basis of time-series complex images. However, in practice, the method in this paper can be further applied to large field differential interferometry processing.
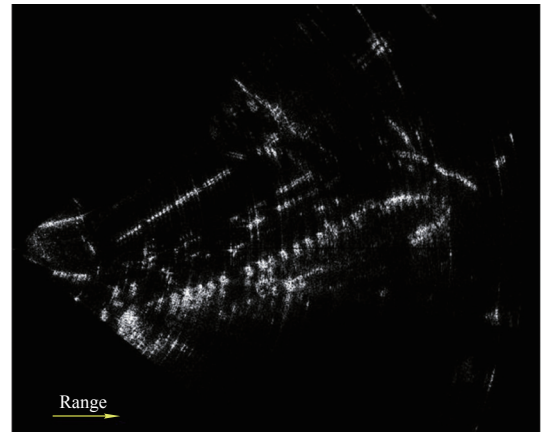

Fig. 22   Imaging result of bridge by the proposed method

Fig. 23 shows the comparison of the imaging results in the traditional mode and the proposed model.
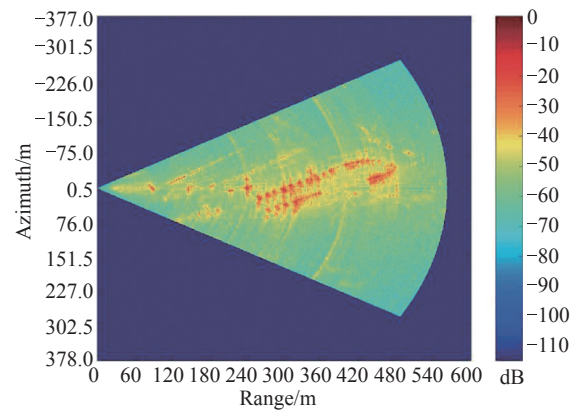
(a) Conventional mode
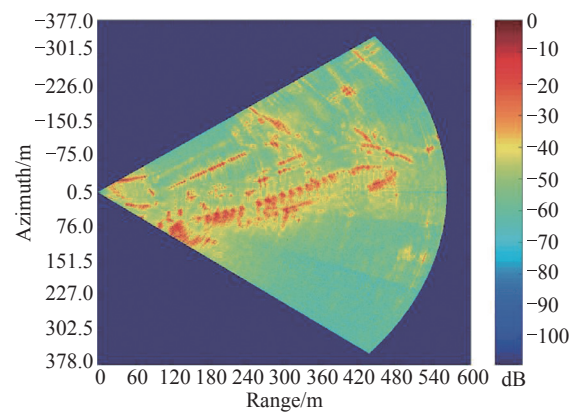
(b) The proposed mode

Fig. 23   Imaging results comparison

The outline of the bridge is more complete after the multi-angle imaging proposed in this paper. As it can be seen from Fig. 23(b), the target information around the bridge is significantly increased.

5. Conclusions

In this paper, the hardware of the existing linear rail GB-SAR system is slightly modified, that is, the turntable is installed on the radar base to realize the acquisition of multi-angle echoes. The large field of view monitoring is realized by joint imaging of multi-angle data in the wave number domain. By deriving the high squint two-dimensional frequency domain expression of echo data, we eliminate the influence of high squint, and then decouple the coupling of azimuth and range frequencies by Stolt interpolation in the wave number domain. Finally, multi-angle data are accumulated to accomplish the large field of view imaging. It is applied to the imaging of the Yongding River Bridge in Beijing that demonstrates the ability of wide-field imaging.

References

[1] ZOU L L, TAKAHASHI K, SATO M. Displacement measurement and monitoring with ground-based SAR: case study at Aratozawa. Proc. of the Asia-Pacific Microwave Conference, 2014: 1022 – 1024.

[2] LUZI G, PIERACCINI M, MECATTI D, et al. Monitoring of an Alpine Glacier by means of ground-based SAR interferometry. IEEE Geoscience and Remote Sensing Letters, 2007, 4(3): 495 – 499.

[3] IGLESIAS R, AGUASCA A, FABREGAS X, et al. Ground-based polarimetric SAR interferometry for the monitoring of terrain displacement phenomena – part II: applications. IEEE Journal of Selected Topics in Applied Earth Observations and Remote Sensing, 2015, 8(3): 994 – 1007.

[4] TARCHI D, OLIVERI F, SAMMARTINO P F. MIMO radar and ground-based SAR imaging systems: equivalent approaches for remote sensing. IEEE Trans. on Geoscience and Remote Sensing, 2013, 51(1): 425 – 435.

[5] YITAYEW T G, FERRO-FAMIL L, ELTOFT T, et al. Tomographic imaging of Fjord ice using a very high-resolution ground-based SAR system. IEEE Trans. on Geoscience and Remote Sensing, 2017, 55(2): 698 – 714.

[6] BAO Q, PENG X M, LIN Y, et al. Suboptimal aperture radar imaging by combination of pseudo-polar formatting and gridless sparse recovery method. Electronics Letters, 2016, 52(9): 765 – 766.

[7] WANG Z, LI Z H, MILLS J. A new approach to selecting coherent pixels for ground-based SAR deformation monitoring. ISPRS Journal of Photogrammetry and Remote Sensing, 2018, 144: 412 – 422.

[8] CROSETTO M, MONSERRAT O, LUZI G, et al. Discontinuous GBSAR deformation monitoring. ISPRS Journal of Photogrammetry and Remote Sensing, 2014, 93: 136 – 141.

[9] LIU B, GE D Q, LI M, et al. Using GB-SAR technique to monitor displacementof open pit slope. Proc. of the IEEE International Geoscience and Remote Sensing Symposium, 2016: 5986 – 5989.

[10] LIU H, KOYAMA C, ZHU J F. et al. Post-earthquake damage inspection of wood frame buildings by a polarimetric GB-SAR system. Remote Sensing, 2016, 8(11): 935 – 946.

[11] LUZI G, NOFERINI L, MECATTI D, et al. Using a ground-based SAR interferometer and a terrestrial laser scanner to monitor a snow-covered slope: results from an experimental data collection in Tyrol (Austria). IEEE Trans. on Geoscience and Remote Sensing, 2009, 47(2): 382 – 393.

[12] TAKAHASHI K, MATSUMOTO M, SATO M. Continuous observation of natural-disaster-affected areas using ground-based SAR interferometry. IEEE Journal of Selected Topics in Applied Earth Observations and Remote Sensing, 2013, 6(3): 1286 – 1294.

[13] PIPIA L, FABREGAS X, AGUASCA A, et al. Polarimetric temporal analysis of urban environments with a ground-based SAR. IEEE Trans. on Geoscience and Remote Sensing, 2013, 51(4): 2343 – 2360.

[14] YUE J P, QIU Z W, WANG X Q, et al. Atmospheric phase correction using permanent scatterers in ground-based radar interferometry. Journal of Applied Remote Sensing, 2016, 10(4): 046013 – 046026.

[15] IGLESIAS R, FABREGAS X, AGUASCA A, et al. Atmospheric phase screen compensation in ground-based SAR with a multiple-regression model over mountainous regions. IEEE Trans. on Geoscience and Remote Sensing, 2014, 52(5): 2436 – 2449.

[16] WANG H Q, MÉRIC S, ALLAIN S, et al. Multi-angular ground-based SAR system for soil surface roughness characterization. Electronics Letters, 2015, 51(15): 1197 – 1199.

[17] WANG Z, LI Z H, MILLS J P. A new nonlocal method for ground-based synthetic aperture radar deformation monitoring. IEEE Journal of Selected Topics in Applied Earth Observations and Remote Sensing, 2018, 11(10): 3769 – 3781.

[18] FORTUNY-GUASCH J. A fast and accurate far-field pseudopolar format radar imaging algorithm. IEEE Trans. on Geoscience and Remote Sensing, 2009, 47(4): 1187 – 1196.

[19] HAN K Y, WANG Y P, CHANG X K, et al. Generalized pseudopolar format algorithm for radar imaging with highly suboptimal aperture length. Science China Information Sciences, 2015, 58(4): 63 – 77.

[20] ZENG T, MAO C, HU C et al. Ground-based SAR wide view angle full-field imaging algorithm based on keystone formatting. IEEE Journal of Selected Topics in Applied Earth Observations and Remote Sensing, 2016, 9(6): 2160 – 2170.

[21] REALE D, SERAFINO F, PASCAZIO V. An accurate strategy for 3-D ground-based SAR imaging. IEEE Geoscience and Remote Sensing Letters, 2009, 6(4): 681 – 685.

[22] MONTI GUARNIERI A, SCIRPOLI S. Efficient wave number domain focusing for ground-based SAR. IEEE Geoscience and Remote Sensing Letters, 2010, 7(1): 161 – 165.

[23] GUO S C, DONG X C. Modified Omega-K algorithm for ground-based FMCW SAR imaging. Proc. of the IEEE 13th International Conference on Signal Processing, 2016: 1647 – 1650.

[24] ZENG T, MAO C, HU C, et al. Grating lobes suppression method for stepped frequency GB-SAR system. Journal of Systems Engineering and Electronics, 2014, 25(6): 987 – 995.

[25] LUO Y H, SONG H J, WANG R, et al. Arc FMCW SAR and applications in ground monitoring. IEEE Trans. on Geoscience and Remote Sensing, 2014, 52(9): 5989 – 5998.

[26] PIERACCINI M, MICCINESI L. ArcSAR: theory, simulations, and experimental verification. IEEE Trans. on Microwave Theory and Techniques, 2017, 65(1): 293 – 301.

[27] WANG R, LOFFELD O, NIES H, et al. Focus FMCW SAR data using the wave number domain algorithm. IEEE Trans. on Geoscience and Remote Sensing, 2010, 48(4): 2109 – 2118.

[28] CARRARAW G, GOODMAN R S, MAJEWSKI R M. Spotlight synthetic aperture radar: signal processing algorithms.

London: Artech House, 1995.
[29] ULANDER L M H, HELLSTEN H, STENSTROM G. Synthetic aperture radar processing using fast factorized back-projection. IEEE Trans. on Aerospace and Electronic Systems, 2003, 39(3): 760−776.

Biographies

ZHANG Yuan was born in 1983. He received his Ph.D. degree from Beihang University in 2017. He was invited by Prof. Xiaoxiang Zhu and Prof. Richard Bamler to conduct Ph.D. joint cultivation at the German Aerospace Center and the Technical University of Munich in 2015 to 2016. Currently, he is an associate professor with the North China University of Technology.
E-mail: zhangyuan@ncut.edu.cn

ZHANG Qiming was born in 1997. He received his B.S. degree in electronic information engineering from Jilin University in 2018. Now he is a postgraduate student of the School of Information Science and Technology, North China University of Technology, Beijing, China. His research interest is synthetic aperture radar imaging.
E-mail: zhangqimingncut@outlook.com

WANG Yanping was born in 1976. He received his Ph.D. degree from the Institute of Electronics, Chinese Academy of Sciences, Beijing, China, in 2003, where he has been the deputy director of the National Key Laboratory of Microwave Imaging Technology. Now he is a professor with the School of Information Science and Technology, North China University of Technology, Beijing, China. He is a member of the IEEE and the IET International Radar Conference Procedure Committee. His research interests include intelligent radar, radar deformation monitoring, and intelligent early warning technology.
E-mail: wangyp@ncut.edu.cn

LIN Yun was born in 1983. She received her Ph.D. degree from the Institute of Electronics, Chinese Academy of Sciences in 2011. From 2012 to 2018, she was with the Institute of Electronics, Chinese Academy of Sciences, as a scientist. Now, she is an associate professor with the School of Electronic Information Engineering, North China University of Technology, Beijing, China. Her current interests are circular SAR imaging and anisotropic scattering target detection.
E-mail: ylin@ncut.edu.cn

LI Yang was born in 1983. He received his Ph.D. degree from the Institute of Electronics, Chinese Academy of Sciences. He is an associate professor with the School of Information Science and Technology, North China University of Technology, Beijing, China. His research interests include intelligent radar, radar deformation monitoring, and intelligent early warning technology.
E-mail: haffner@126.com

BAI Zechao was born in 1991. He is currently pursuing his Ph.D. degree at North China University of Technology, Beijing. His research interests are the spaceborne/ground interferometric synthetic aperture radar (InSAR) algorithm and its application in geological disaster InSAR data processing.
E-mail: baizechao1991@163.com

LI Fang was born in 1986. He received his Ph.D. degree in photogrammetry and remote sensing from the Technical University of Munich. He is an associate research fellow with the Quanzhou Institute of Equipment Manufacturing, Haixi Institutes, Chinese Academy of Sciences, Quanzhou, China. His main research interests include image processing and analysis, pattern recognition, and related remote sensing/environmental and industrial applications.
E-mail: fangli@fjirsm.ac.cn